NMR Backbone Dynamics of the Human Type I Interferon Binding Subunit, a Representative Cytokine Receptor†

Jordan H. Chill,* Sabine R. Quadt, and Jacob Anglister

Department of Structural Biology, Weizmann Institute of Science, Rehovot 76100, Israel

Received February 26, 2004; Revised Manuscript Received May 19, 2004

ABSTRACT: The antiviral and antiproliferative activities of type I interferons (IFNs) are mediated by a common receptor, and its second subunit (IFNAR2) exhibits nanomolar affinity to both IFNα and IFNβ subtypes. We have previously determined the structure of the IFN-binding extracellular domain of IFNAR2 (IFNAR2-EC) using multidimensional NMR [Chill, J. H., Quadt, S. R., Levy, R., Schreiber, G. E., and Anglister, J. (2003) *Structure 11*, 791−802], showing it to comprise two fibronectin domains linked by a hinge. As the first cytokine receptor structure determined in the unliganded state and in solution, IFNAR2-EC offers an opportunity to characterize the dynamics of the cytokine receptor family and their correlation to biological function. Backbone dynamics of IFNAR2-EC were investigated using ^{15}N relaxation at 11.74 and 18.79 T, and measurements of residual dipolar couplings (RDCs). Dynamics of the binding site distinguish between rigid structural domains, which stabilize the binding site conformation, and a more flexible binding interface which interacts with the ligand. Measurements of diffusional anisotropy and RDCs and model-free analysis all show that the backbone of the hinge interdomain region of IFNAR2-EC is rigid on the picosecond to nanosecond time scale. Signal transduction in cytokines receptors is initiated by ligand-induced juxtaposition of the two receptor subunits, triggering the mutual phosphorylation of kinases associated to their cytoplasmic domains. The rigidity of the hinge ensures correct positioning of the receptor subunits in the ternary signaling complex and modulates the interaction between kinases in the cytoplasm, thereby controlling the rate and efficiency of phosphorylation.

Type I interferons (IFNs)[1] assume a pivotal role in several important cellular processes, notably, inhibition of cell growth and viral replication and control of apoptosis (*1*). These activities have motivated extensive biomedical research focused upon the biology of IFNs and their potential pharmaceutical applications (*2*). Currently, IFNs are widely used for treatment of several viral diseases, notably, hepatitis (*3*), various types of cancer (*4*, *5*), relapsing-remitting multiple sclerosis (*6*), and, recently, arthritis (*7*). The cellular activity of type I IFNs is mediated by a common receptor, consisting of two subunits, IFNAR1 (*8*) and IFNAR2 (*9*), both members of the class II helical cytokine receptor (HCR) family (*10*). Each receptor subunit consists of a ligand-binding extracellular repeat of fibronectin (FNIII) domains (four and two for IFNAR1 and IFNAR2, respectively), a single membrane spanning domain, and an intracellular domain.

The crucial step of the IFN signaling cascade is the formation of the ternary complex between IFNAR1, IFNAR2, and the IFN ligand, which assembles in sequential fashion. Initially, IFNAR2 binds type I IFNs with nanomolar affinity to form the IFNAR2/IFN complex. This intermediate then recruits the IFNAR1 subunit into a ternary complex, for which affinity increases up to 20-fold. Notably, the intrinsic affinity of IFNAR1 to type I IFNs is low (K_D > 100 nM). Upon formation of the ternary assembly, the IFN signal is transported to the nucleus by way of a phosphorylation cascade involving the intracellular domains of the two subunits (*11*). Key participants in this process are tyrosine kinase 2 (Tyk2) and Janus kinase 1 (Jak1), which are preassociated with the cytoplasmic domains of IFNAR1 and IFNAR2, respectively, and signal transducers and activators of transcription (STATs) bound to IFNAR2. After mutual cross-phosphorylations of Jak1 and Tyk2, the final outcome of this pathway is a heterodimer of phosphorylated STAT1 and STAT2, which dissociates from the receptor and is transported into the cell nucleus (*1*, *12*).

This sequence of events—ligand-binding by a high-affinity subunit, association of a low-affinity subunit into a ternary complex, followed by an intracellular cross-phosphorylation cascade—is common to the members of the cytokine receptor superfamily. The structures of several of these receptors have been solved by X-ray crystallography. Notable examples are the growth hormone (GHR) (*13*), the prolactin (PRLR) (*14*),

† This study was supported by the Israel Academy of Science and by NIH grant GM53329 (J.A.). J.A. is the Dr. Joseph and Ruth Owades Professor of Chemistry.

* To whom correspondence should be addressed. Tel: 972-8-9342152. Fax: 972-8-9344136. E-mail: jordan.chill@weizmann.ac.il.

[1] Abbreviations: CSA, chemical shift anisotropy; DD, dipole−dipole interaction; EPOR, erythropoietin receptor; FNIII, fibronectin-III module; GHR, growth hormone receptor; HCR, helical cytokine receptor; hetNOE, heteronuclear ^{15}N-{^{1}H}-NOE; HSQC, heteronuclear single-quantum coherence; IFN, interferon; IFNAR2, subunit 2 of the IFN-α receptor; IFNAR2-EC, extracellular domain of IFNAR2; IFNγR, IFN-γ receptor; IL-10R, interleukin-10 receptor; ms, millisecond; NOE, nuclear Overhauser effect; NOESY, NOE spectroscopy; NMR, nuclear magnetic resonance; ns, nanosecond; ppm, parts per million; PRLR, prolactin receptor; ps, picosecond; R_1, longitudinal relaxation time; R_2, transverse relaxation time; RDC, residual dipolar coupling; rmsd, root-mean-square deviation.

10.1021/bi049606g CCC: $27.50 © 2004 American Chemical Society
Published on Web 07/17/2004

the erythropoietin (EPOR) (*15*), the interleukin-10 (IL-10R) (*16*), and the IFN-γ receptors (IFNγR) (*17*). All members of this receptor superfamily share the double FNIII motif in their extracellular ligand-binding domains. The interactions between cytokines and receptor subunits have been studied extensively. Despite the overall similarity of their signaling processes, it is the nature of the pivotal ternary signaling complex that determines the characteristics of receptor biological activity. Differences in the affinity and duration of the receptor−ligand interaction (*18*, *19*), as well as extracellular (*16*, *19*) and intracellular (*18*) organizational diversity of the signaling complexes between receptors are factors influencing signaling processes by different ligands.

The biological function of proteins is often related to their dynamic properties (*20*). However, since cytokine receptor structures have been invariably solved by X-ray crystallography, this aspect of their activity has not been explored. Furthermore, most receptors could not be crystallized in the unliganded state, further limiting the ability to understand the factors governing the formation of the signaling complex. The structure of IFNAR2-EC, a stable 25-kDa polypeptide that retains the full binding activity of IFNAR2 (*21*) was recently elucidated by NMR, representing the first cytokine receptor structure determined in its free state and in solution (*22*). It therefore provides an opportunity to investigate the dynamic behavior of these receptors. Study of IFNAR2-EC is of particular interest due to its several unique characteristics. Whereas receptor binding sites typically involve loop segments from both FNIII domains (N- and C-domains), the IFNAR2-EC binding site has been mapped by mutagenesis (*23*, *24*), immunoblocking (*25*), and NMR (*26*) studies to a contiguous surface formed by N-domain loops only. The lack of C-domain involvement is consistent with the perpendicular interdomain orientation observed for IFNAR2-EC (*22*), which retracts the C-domain loops from the binding surface upon the N-domain. An inherent flexibility of the IFNAR2-EC binding surface has been suggested by its aliphatic character (*22*) and supported by a previously observed ligand-induced tightening of the N-domain of IFNAR2-EC, which was not limited to the binding site (*26*). In contrast, intermolecular interactions involving key aromatic residues appear to be required for signaling in other receptors. This distinction is important in light of the cross-reactivity of IFNAR2, which exhibits comparable affinity with all IFNα isotypes and IFNβ (*24*). Binding sites of these ligands have been shown to overlap, but differ in contribution of the various residues to binding energy (*23*, *27*). The ability of IFNAR to mediate distinct and ligand-specific signaling profiles remains enigmatic to date (*28*−*30*).

Dynamical properties of biomacromolecules in solution can be described by measuring relaxation rate constants of backbone amide ^{15}N nuclei, typically, longitudinal and transverse autorelaxation rates R_1 and R_2, and the heteronuclear ^{15}N-{^{1}H}-NOE (hetNOE), and analyzing the results based on a model of molecular motion (*31*−*33*). ^{15}N-relaxation data is typically interpreted in the context of the model-free approach (*34*). The relaxation rates are determined by the overall global tumbling time, typically on the ns time scale for proteins, and one (in the original model-free approach) (*34*) or two (in the extended model-free approach) (*35*) local motions. The traditional model-free approach assumes that the dynamics of backbone ^{1}H-^{15}N bond-vectors is described by generalized order parameters, S_f^2 and S_s^2, describing the amplitude of motion, and correlation times τ_i and τ_f. In this manner, ^{15}N relaxation measurements provide residue-specific information on the dynamic behavior of the protein backbone.

In this study, we use NMR to investigate the dynamics of the 25-kDa IFNAR2-EC (212 residues). ^{15}N spin relaxation rates were measured at 11.74 and 18.79 T for backbone amides of IFNAR2-EC. Model-free-based analysis of the relaxational data, together with residual dipolar coupling (RDC) measurements, shed light upon IFNAR2-EC backbone dynamics. Dynamics of the IFNAR2-EC binding site reveal highly flexible loop segments and a malleable binding surface interacting with the IFN ligand supported by a more rigid scaffold which stabilizes the binding site conformation. The interdomain hinge region, located at the heart of the interface between the two FNIII domains, is shown to be rigid on the picosecond to nanosecond time scale. This rigidity indicates that ligand binding does not involve changes in the interdomain orientation, and may ensure efficient signaling by optimally orienting the components of the signaling complex. As a first report on the dynamics of a free hematopoietic receptor in solution, this study not only illuminates important features of IFNAR2-EC function, but may provide previously unavailable information on the dynamic behavior of related receptors.

MATERIALS AND METHODS

Sample Preparation. Expression and purification of ^{15}N-labeled IFNAR2-EC, as well as preparation of the ^{15}N-IFNAR2-EC/U-IFNα2 complex, are described elsewhere (*26*). NMR samples were prepared in 20 mM deuterated Tris buffer (pH 8.0) with 0.02% sodium azide and 5% D_2O. Protein concentrations were 0.25−0.3 mM. Weakly aligned samples of ^{15}N-IFNAR2-EC in H_2O were prepared in polyacrylamide gel (monomer:cross-linker ratio of 37.5:1) swelled with a solution of the protein as previously described (*36*, *37*). Longitudinal pressure was applied on the swelled gel in a Shigemi NMR tube using the insert.

NMR Spectroscopy. NMR spectra were recorded on Bruker DMX 500 MHz (cryoprobe-equipped) and DRX 800 MHz spectrometers, using triple-resonance probes including *z*-axis and triple axis gradients, respectively. All measurements of ^{15}N relaxational parameters were performed at 304 K. Sample temperature was verified using a standard calibration sample of 80% ethylene glycol in DMSO-d_6. Quadrature detection was obtained using the States-TPPI method (*38*). Pulsed field gradients were used to suppress magnetization originating from water or unwanted transfer pathways. ^{15}N decoupling during acquisition was effected using a GARP decoupling sequence. Water suppression was effected using a WATERGATE block (*39*). In all experiments, the ^{1}H carrier coincided with the H_2O signal, and the ^{15}N carrier was set at 118 ppm and referenced as described previously (*40*). Processing and analysis of NMR data and peak-picking were performed on an Octane station (Silicon Graphics) using XWINNMR 3.1 (Bruker Biospin) and the NMRPipe/NMRDraw package (*41*).

^{15}N Relaxation Measurements. Measurements of R_1, R_2, and hetNOEs were performed using previously reported sequences (*42*−*44*), including H_2O flip-back pulses (*44*, *45*) to minimize water saturation. Complex points acquired were

Table 1: ^{15}N Relaxation Rates, NOEs, and Order Parameters at 500 and 800 MHz[a]

	500 MHz				800 MHz			
residues	R_1	R_2	NOE	S^2	R_1	R_2	NOE	S^2
core[b]	1.01 ± 0.03	16.6 ± 0.7	0.75 ± 0.04	0.79 ± 0.03	0.60 ± 0.02	22.2 ± 0.9	0.79 ± 0.05	0.85 ± 0.03
core[c] (N)	1.03 ± 0.03	16.3 ± 0.7	0.74 ± 0.04	0.79 ± 0.03	0.61 ± 0.02	21.6 ± 0.9	0.79 ± 0.05	0.85 ± 0.03
core[c] (C)	1.03 ± 0.03	16.3 ± 0.7	0.75 ± 0.04	0.79 ± 0.03	0.60 ± 0.02	21.7 ± 0.9	0.80 ± 0.05	0.84 ± 0.03
hinge[d]	0.99 ± 0.03	17.2 ± 0.7	0.74 ± 0.04	0.79 ± 0.02	0.58 ± 0.03	23.2 ± 0.9	0.77 ± 0.04	0.86 ± 0.03
loops	1.03 ± 0.04	15.3 ± 0.7	0.54 ± 0.04	0.71 ± 0.03	0.67 ± 0.03	20.8 ± 0.9	0.62 ± 0.05	0.78 ± 0.03
termini	1.20 ± 0.05	8.7 ± 0.7	0.20 ± 0.03	0.36 ± 0.02	0.98 ± 0.05	8.7 ± 0.7	0.19 ± 0.03	0.28 ± 0.03

[a] Measured R_1 and R_2 rates (in s^{-1}) and NOE values, and order parameters derived from model-free analysis, are listed for various domains of IFNAR2-EC. Standard deviations (based upon Monte Carlo simulations) for each value are presented as well. [b] Core residues were defined as residues with NOE > 0.65 (0.70) at 500 (800) MHz and located in a well-defined secondary element. [c] N- and C-domains include residues 13−100 and 111−203, respectively. [d] Hinge residues include the S106−F107−E108 segment and all residues whose HN bond-vector lies within a 7 Å radius from it. This includes 19 residues: 16−22, 104−111, 183, 185, 194 and 196. Of these, relaxation data was unavailable for N20 (below detection level), M105 (overlap), and the two prolines P109 and P110.

1024 and 120−140 (180−200), and spectral widths were 6.98 (11.16) and 1.218 (1.95) kHz in the F_2 and F_1 dimensions, respectively, for the 11.74 (18.79) T field. A total of 32−80 transients per t_1 experiment were acquired for measurements of R_1 and R_2. R_1 measurements were based on seven (six) collected timepoints with parametric delays of 24−1560 (24−2160) ms on the 500 (800) MHz spectrometers. R_2 measurements were similarly based on six collected timepoints with parametric delays of 8−80 (8−72) ms. The delay between scans was set at 1.6 (2.0) s. Data from the relaxation experiments were apodized with a cosine (cosine-bell) window function in t_1 (t_2). The determination of uncertainties in peak intensity was based upon S/N ratios in the spectra. hetNOEs were determined by recording pairs of interleaved spectra with and without proton saturation during the recycle delay. Saturation was achieved by applying a 120° ^{1}H-pulse every 5 ms. A total of 96 transients were collected per t_1 experiment and delays between scans were 6.0 s. Data were processed as described for R_1 and R_2 measurements.

Calculation of Relaxation Parameters. Peak intensities at different delays in R_1, R_2, and hetNOE measurements were obtained using NMRDraw Tcl peak-picking scripts (*41*). R_1 and R_2 values were determined by nonlinear least-squares fitting of the data to an exponential curve $I(t) = I_0 \exp(-R_j t)$ ($j = 1, 2$) using the modelXY package (*41*) and in-house MATLAB scripts. Uncertainties in R_1 and R_2 values were estimated by Monte Carlo simulations (*43*). hetNOEs were estimated by calculating the ratio of intensities in spectra recorded with and without proton saturation, and errors extracted from the uncertainties of the individual measurements.

Hydrodynamic Calculations. The inertia tensor of IFNAR2-EC (PDB accession code 1N6V (*22*)) was calculated using the program PDBINERTIA (A. Palmer, Columbia University). Hydrodynamic analysis for IFNAR2-EC was performed at 304 K using HYDRONMR (*46*). Viscosity was assumed to be 0.80 cP, based upon a viscosity of 0.78 for H_2O at 304 K, protein concentration of 8 mg/mL, specific volume of 0.75 mL/g, and a shape factor of $k \sim 4$ (*47*).

Anisotropic Global Diffusion. Interpretation of ^{15}N-relaxation data is greatly complicated by the presence of diffusional anisotropy in the examined protein. In such systems, ^{15}N relaxation is heavily dependent upon the orientation of the ^{1}H-^{15}N bond-vector relative to the diffusional tensor. Reduced sets of R_2/R_1 ratios were created, in which local-motion- and conformational-exchange-affected residues were eliminated (*48*−*50*). These served as input for calculation of the diffusion tensor for overall rotational reorientation using the R2R1_DIFFUSION (A. Palmer, Columbia University) and ROTDIFF (*51*) programs. Monte Carlo simulations of errors and graphic presentation of the results employed the program TENSOR2 (*52*).

Table 2: Diffusion Tensor Parameters of IFNAR2-EC at 11.74 T

domain[a]	HN sites	D_{iso}[b] (10^7 s^{-1})	$D_\parallel/D_\perp$[b]	θ (deg)[c]	φ (deg)[c]
all	78	1.09 ± 0.04[d]	1.59 ± 0.05	14 ± 2	241 ± 6
N-domain	41	1.08 ± 0.04	1.63 ± 0.08	15 ± 3	258 ± 12
C-domain	37	1.08 ± 0.04	1.67 ± 0.09	16 ± 3	229 ± 12

[a] Domains were defined as residues 1−106 (N-domain) and 107−212 (C-domain). [b] For a prolate axial rotator with diffusion tensor with elements D_{zz}, D_{yy}, D_{xx}, $D_\parallel = D_{zz}$, $D_\perp = D_{yy} = D_{xx}$. $D_{iso} = (D_\parallel + 2D_\perp)$, and is inversely related to the global tumbling time, $D_{iso} = (6\tau_c)^{-1}$. [c] Polar angles (θ, φ) describing the orientation of the unique diffusion axis D_{zz} in the inertial frame of IFNAR2-EC. The angle between unique axes of the inertia and diffusion tensors (θ) is ∼15°. [d] Errors were estimated using Monte Carlo simulations.

Model-Free Analysis of Relaxation Data. The expressions for ^{15}N heteronuclear relaxation parameters R_1, R_2, and hetNOE are well known (*53*) and will not be reiterated here. The average internuclear ^{1}H-^{15}N distance r_{NH} was assumed to be 1.02 Å and the ^{15}N chemical shift anisotropy (CSA) tensor was approximated to −172 ppm, and assumed to be axially symmetric and coaxial with the dipolar interaction (*54*). Model-free analysis was performed using the programs DYNAMICS (*55*, *56*) and ModelFree4.0 (*57*). Relaxation rate constants were fitted to five different models of motion (see Table 2) following the protocol outlined by Mandel et al. (*57*).

Residual Dipolar Coupling Measurements and Analysis. RDCs for backbone ^{1}H-^{15}N moieties were estimated by comparing the DSSE-[^{1}H,^{15}N]-IPAP−HSQC spectra (*58*) acquired at 18.79 T and 308 K for IFNAR2-EC in isotropic and anisotropic samples. Complex points acquired were 2048 and 200, and spectral widths were 9.62 and 1.95 kHz in the F_2 and F_1 dimensions, respectively. A total of 16 transients per t_1 experiment were acquired in interleaved fashion, and split later into the two spectra using XWINNMR (Bruker). Data were apodized with a cosine (cosine-bell) window function in t_1 (t_2). Peak-picking and extrapolation of RDCs was performed using NMRView (*59*). Couplings were normalized by dividing all values by the order parameter S

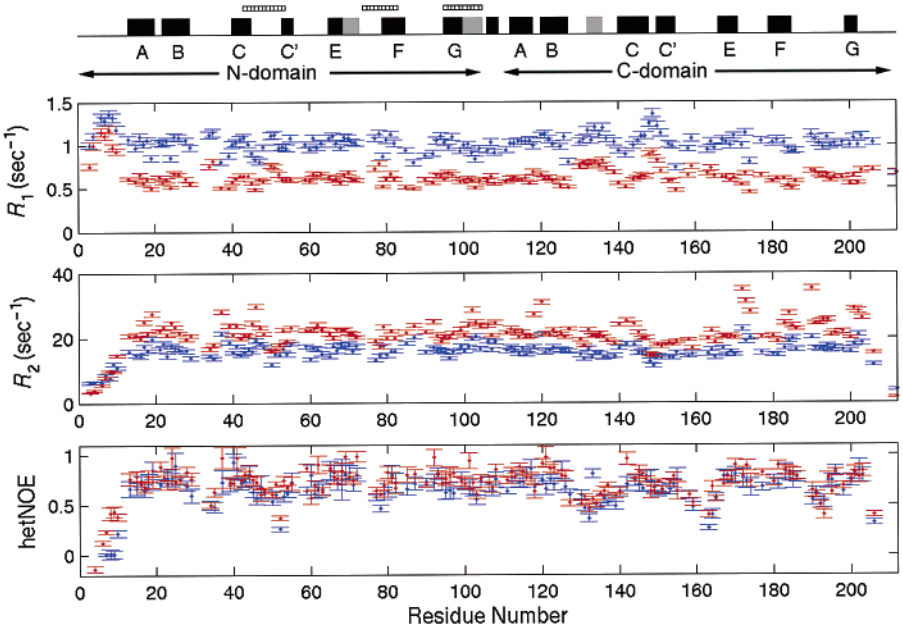

FIGURE 1: Relaxation measurements for IFNAR2-EC. (Top) R_1, (middle) R_2, and (bottom) ^{1}H-^{15}N NOEs for backbone ^{15}N nuclei of IFNAR2-EC. Data obtained at 500 and 800 MHz are indicated in blue and red, respectively, with bars indicating Monte Carlo estimated errors. Secondary structure elements appear above, with β-strands and α-helices designated by black and gray bars, respectively. Segments of IFNAR2-EC forming the ligand binding site are marked with hatched bars.

obtained from the model-free analysis at 18.79 T. The cumulative error of normalized couplings was estimated at 4 Hz. Fitting of alignment tensors and error analysis were performed using the program MODULE (*60*).

RESULTS

Backbone ^{15}N Relaxation Rates of IFNAR2-EC. ^{15}N R_1, R_2, and hetNOE measurements were conducted for IFNAR2-EC at 11.74 and 18.79 T. Of the 201 nonproline residues of IFNAR2-EC, 183 could be detected in the ^{1}H-^{15}N-HSQC spectrum and assigned, and only 173 could be detected with sufficient precision to be used in the spin relaxation study. Missing residues were invariably located in loop segments of the structure, and their absence is attributed to broadening by solvent exchange beyond the detection limit (*26*). Following a strict policy of excluding fully or partially overlapping peaks from the analysis, 13 pairs of such peaks were omitted, leaving 147 available backbone ^{1}H-^{15}N sites which were analyzed. Relaxation rates acquired at both fields are summarized in Figure 1. Average values and errors calculated by Monte Carlo simulation for various domains of IFNAR2-EC appear in Table 1. Typically, errors were on the order of 4% for R_1 and R_2, and 8% for hetNOE measurements.

A few general observations emerge from the data. The hetNOE is the most sensitive parameter to local motions. Indeed, regions of lower NOE values closely correlate with loop segments. This is particularly evident for the BC_N, CC'_N, BC_C, $C'E_C$, and FG_C loops; the two BC loops are the longest and least ordered in the IFNAR2-EC structure. (Labeling of β-strands of IFNAR2-EC A−G follows the convention for immunoglobulin folds, and loops are referred to by their adjacent β-strands; the two FNIII domains are designated by a subscript N or C.) The hinge region and interdomain interface were found to have relaxation rates similar to those found in the hydrophobic cores of the FNIII domains. Data for the two terminal segments clearly demonstrate they are unstructured, a finding consistent with the averaged RDCs and lack of long-range NOEs observed for these regions (*22*). Several residues exhibit a significantly higher (20−60%) R_2 rate when compared to the average value. Since IFNAR2-EC is elongated in shape, these variations in relaxation rates do not necessarily evidence backbone mobility, but may result from the anisotropic tumbling of the protein.

Global Diffusion Anisotropy. Relative principal values of the IFNAR2-EC inertia tensor are 1.00:0.88:0.31. Therefore, IFNAR2-EC may be described to a first approximation as an axially symmetric body with $I_\parallel/I_\perp \sim 3$. The unique inertial axis lies along an imaginary line connecting the hydrophobic cores of both FNIII domains (Figure 2). Using the empirical relation which holds for prolate ellipsoids $D_\parallel/D_\perp \approx (I_\parallel/I_\perp)^{-0.707}$ (*61*), a diffusional anisotropy of ∼2.1 would be predicted for IFNAR2-EC. However, the surrounding hydration layer of solvent decreases the effective anisotropy of the diffusional tensor. The program HYDRONMR (*46*, *62*) yielded typical $D_\parallel/D_\perp$ ratios of 1.9 ± 0.1 for an aqueous viscosity of 0.80 cP, in agreement with the elongated structure of IFNAR2-EC.

Properly filtered R_2/R_1 ratios were used to determine the rotational diffusion tensor of IFNAR2-EC. Of 147 residues with full sets of relaxation parameters, 80 met the trimming criteria (NOE > 0.65, well-defined structure), 78 of which were used to fit the diffusion tensor to the R_2/R_1 data. For data acquired at 11.74 T this analysis yielded an apparent global tumbling time of 15.3 ± 0.4 ns, and an anisotropy ratio of 1.59 ± 0.05 for the prolate IFNAR2-EC molecule. The diffusion and inertia tensors formed an angle of ∼15° between their unique axes (Figure 2). The axial model was preferred over the isotropic model, ($F = 37.1$, or $P < 10^{-14}$), while a fully anisotropic model was not sufficiently supported by the data ($P \sim 0.07$). Data at 18.79 T was in general agreement with these results, but was less amenable to proper filtering since exchange contributions scale quadratically with

Table 3: Model-Free Analysis of Relaxation Parameters at 500 and 800 MHz[a]

	500 MHz								800 MHz							
	model[c]					S^2	τ_i[d] (ps)	R_{ex} (s^{-1})	model[c]					S^2	τ_i[d] (ps)	R_{ex} (s^{-1})
	1	2	3	4	5				1	2	3	4	5			
all	61	32	8	17	27				74	20	9	8	34			
core[b]	53	17	3	2	0	0.79 ± 0.03	30 ± 10 [19]		61	9	3	2	0	0.85 ± 0.03	27 ± 10 [11]	
hinge[b]	12	0	2	1	0	0.79 ± 0.03			13	1	1	0	0	0.86 ± 0.03		
loops[b]	8	15	3	14	21	0.71 ± 0.03	30 ± 8[e] [29] 1300 ± 250[f] [21]	3.6 ± 0.9 [17]	13	11	6	7	24	0.78 ± 0.03	100 ± 20[e] [18] 800 ± 120[f] [24]	7 ± 1.3 [13]

[a] Average values of fitted dynamic parameters in various domains are shown. Errors were calculated from Monte Carlo simulations. [b] Domain definitions are identical to those in Table 1. [c] Presented are the number of residues assigned to each of the models of molecular motion. Relaxation rates were fitted to five models as in ref 55, yielding the order parameter S^2, internal motion correlation time τ_i, and exchange contribution R_{ex}. Fitted parameters in the various models are model 1 − S^2; model 2 − S^2, τ_i; model 3 − S^2, R_{ex}; model 4 − S^2, τ_i, R_{ex}; model 5 − S_s^2 (order parameter for slow motion), S_f^2 (order parameter for fast motion, $S^2 = S_s^2 S_f^2$), τ_i. [d] In models 2 and 4 τ_i represents a fast local motion, whereas in model 5 it represents a slow local motion and fast motions are assumed to bear a negligible effect upon relaxation. The number of residues for which the average values was calculated appears in square brackets. Averages of sparsely populated models are considered statistically insignificant and are omitted. [e] Calculated for residues assigned to models 2 and 4. [f] Calculated for residues assigned to model 5.

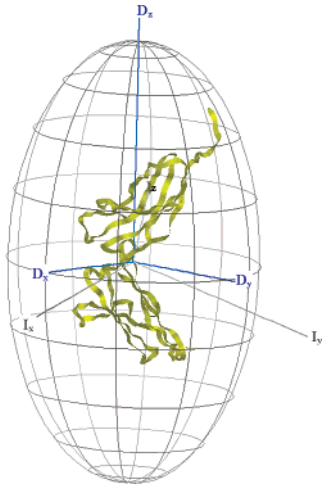

FIGURE 2: Inertia and diffusion tensors of IFNAR2-EC. The principal axes of the optimal diffusion tensor (blue, denoted $D_{x,y,z}$) and the inertia tensor (gray, denoted $I_{x,y,z}$) of IFNAR2-EC are shown. The two unique axes, I_z and D_z, form an angle of ~15°. Properly trimmed R_2/R_1 data acquired at 500 MHz for 78 sites in the IFNAR2-EC backbone were used to calculate the optimized rotational diffusion tensor. The figure was created using the program TENSOR2 (*52*).

the external field strength. Therefore, the diffusion tensor obtained from the 11.74 T data alone was used in the ensuing model-free analysis. The discrepancy between fitted (~1.6) and predicted (1.9) $D_\parallel/D_\perp$ ratios may result from deviations from a prolate ellipsoid shape, an underestimated solvation layer, or from the presence of unstructured segments at the termini of IFNAR2-EC (*44*).

The correlation between R_2/R_1 ratios in anisotropically tumbling proteins and the ^{1}H-^{15}N bond-vector orientation presents a source of long-range structural information that has been used for the refinement of structure (*51*). We utilized this property to validate the interdomain orientation of IFNAR2-EC. Data acquired at 11.74 T were divided into two sets, containing R_2/R_1 ratios for the N- and C-domains of IFNAR2-EC. Each set was analyzed separately and fit to a rotational diffusion tensor without further filtering as described above. The differences between τ_C and $D_\parallel/D_\perp$ for the two tensors obtained were below the experimental error. Furthermore, the unique axes of diffusion as predicted by each dataset and were collinear at the level of accuracy obtained in the fit (Table 2). These findings strongly argue that the two domains tumble as a single entity, and therefore are connected by a rigid hinge domain. It also follows that R_2/R_1 ratios are not consistent with an interdomain angle of 120−130° as is seen in IFNγR, but rather support our previously reported perpendicular interdomain orientation (*22*).

Model-Free Approach Accounting for Axial Global Diffusion. The Lipari-Szabo model-free approach (*34*) was used to analyze the backbone relaxation data, following well-established protocols (*57*). The analysis was performed using the DYNAMICS (*55*, *56*) and ModelFree4.0 (*57*) programs, which consider anisotropic tumbling throughout the model selection process. Optimal values of τ_C, $D_\parallel/D_\perp$, θ and φ of the global diffusion tensor were employed as initial conditions for calculations, and further optimized in iterative fashion after model selection. Final values used were τ_C(app) = 15.3 ns, $D_\parallel/D_\perp = 1.58$ for the 11.74 T data, and τ_C(app) = 14.7 ns, $D_\parallel/D_\perp = 1.54$ for the 18.79 T data. Both programs yielded highly similar results, and the model-free analysis converged for practically all analyzed residues. The microdynamic parameters derived from this analysis (generalized order parameter S^2, internal motion correlation time τ_i, and exchange rate R_{ex}) are shown in Figures 3 and 4. Average S^2 values for various domains of interest in IFNAR2-RC appear in Tables 1 and 3.

The profiles of model selection and microdynamic parameters are very similar in the two datasets (Table 3). The majority of residues in structured regions (~90% for both datasets) are assigned to model 1 or model 2 with short (<30 ps) τ_i values (hereby collectively referred to as rigid models). In contrast, several residues in loop segments (35−40%) are fitted to model 5 (the Clore extended model) (*35*), indicating a reorientation of a protein or motions of the protein main chain with a correlation time of 0.2−2 ns. Residues 150−153 are assigned to this model, suggesting a long CC′$_C$ loop and short C′$_C$ β-strand as observed for the N-domain. Residues of the two unstructured termini (residues 3−10 and 206−212) are invariably fitted to this model as well. No difference of statistical significance in model selection was observed between the two domains of IFNAR2-EC. Average values for S^2 are 0.79 ± 0.03 (0.85 ± 0.03) for the core regions of IFNAR2-EC, and 0.66 ± 0.04 (0.71 ± 0.03) for the flexible regions in the data acquired at 11.74 (18.79) T.

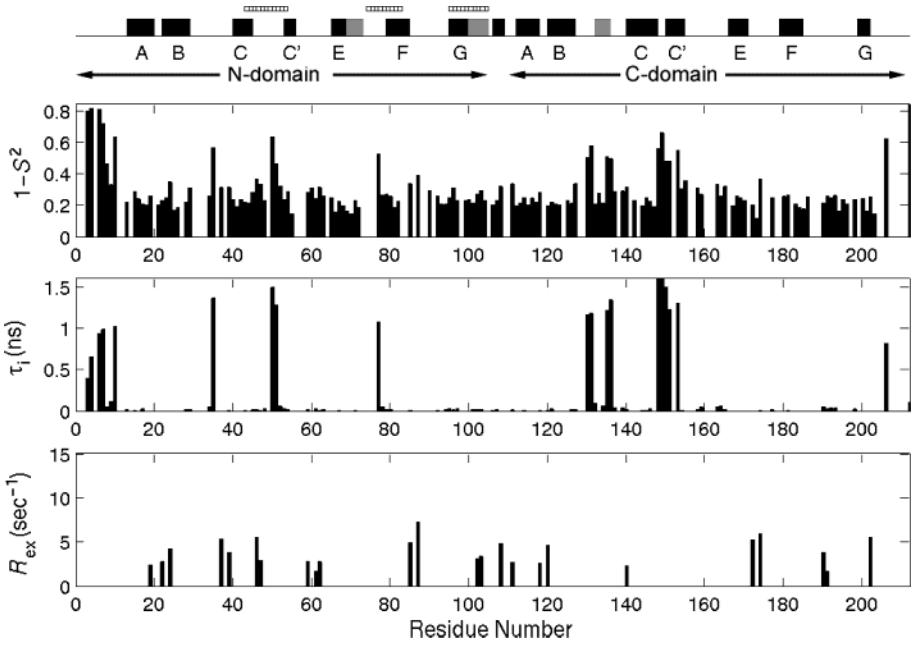

FIGURE 3: Model-free analysis of relaxation measurements at 11.74 T. Microdynamic parameters calculated for 147 backbone sites of IFNAR2-EC by model-free analysis of relaxation data using the axial diffusional model. Top, relative mobility of a given residue expressed as $(1 - S^2)$, where S^2 is the generalized order parameter. Middle, internal correlation times τ_i for residues assigned to models 2, 4 (small bars, < 0.15 ns), and 5 (large bars, > 0.5 ns). Bars for residues E148 and G149 exceed 1.6 ns and are truncated for clarity of presentation. Bottom, exchange contributions R_{ex} (in s^{-1}). Secondary structure elements appear above, with β-strands and α-helices designated by black and gray bars, respectively. Segments of IFNAR2-EC forming the ligand binding site are marked with hatched bars.

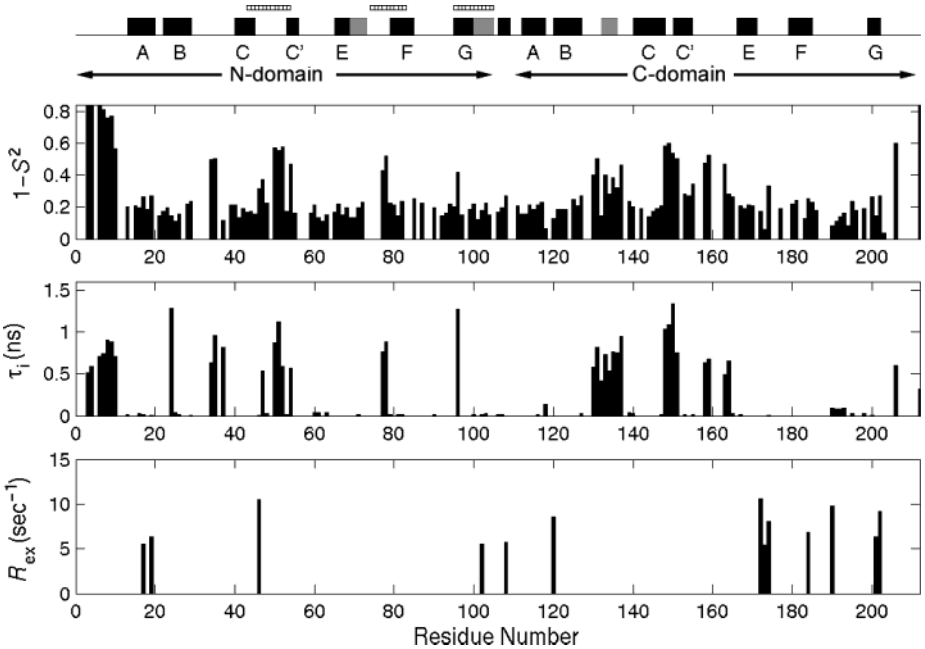

FIGURE 4: Model-free analysis of relaxation measurements at 18.79 T. Microdynamic parameters calculated for 147 backbone sites of IFNAR2-EC by model-free analysis of relaxation data using the axial diffusional model. Top, relative mobility of a given residue expressed as $(1 - S^2)$, where S^2 is the generalized order parameter. Bars for residues of the mobile terminal segments are truncated for clarity of presentation. Middle, internal correlation times τ_i for residues assigned to models 2, 4 (small bars, < 0.15 ns), and 5 (large bars, > 0.5 ns); Bottom, exchange contributions R_{ex} (in s^{-1}). Secondary structure elements appear above, with β-strands and α-helices designated by black and gray bars, respectively. Segments of IFNAR2-EC forming the ligand binding site are marked with hatched bars.

Of particular interest is the interdomain region, an interface between the two FNIII domains measuring 1000−1100 Å^2 for various HCRs. At the heart of this hydrophobic region lies the three-residue segment S106-F107-E108, which forms a parallel β-strand interacting with the ABE_N β-sheet, a motif common to all type II HCRs. Residues of the hinge region (defined as the 106−108 segment and ^{1}H-^{15}N bond-vectors within a 7 Å radius around it) average an S^2 of 0.79 ± 0.03 (0.86 ± 0.03) for 500 (800) MHz data. The vast majority of hinge residues (12 of 15) are assigned to model 1. Residues S17, R22, and E108 are the only residues containing an exchange contribution to their relaxation. Another intriguing region is the IFN binding site, comprised of the CC'_N, EF_N loop segments and interdomain helix. Residues D50-E51-L52 of the CC'_N loop, and residues E77−A78 of the EF_N loop, which form the binding site for IFN, are characterized

Table 4: Alignment Tensor Parameters of IFNAR2-EC

domain[a]	$^1D_{HN}$ couplings	D_a (Hz)[b]	D_r (Hz)[b]	α (deg)[c]	β (deg)[c]	γ (deg)[c]
all	110	-6.3 ± 0.3[d]	-3.6 ± 0.4	48 ± 14	172 ± 2	131 ± 13
N-domain	52	-6.4 ± 0.4	-3.4 ± 0.5	47 ± 21	171 ± 3	129 ± 20
C-domain	58	-6.0 ± 0.5	-3.9 ± 0.4	47 ± 20	174 ± 3	128 ± 20

[a] Domains were defined as residues 1−106 (N-domain) and 107−212 (C-domain). [b] The axial and rhombic components of the alignment tensor are defined as $D_a = D^m[A_{zz} - (A_{xx} + A_{yy})/2]/3$ and $D_r = D^m(A_{xx} - A_{yy})/3$. $|A_{zz}| > |A_{yy}| > |A_{xx}|$ are the elements of the diagonalized alignment tensor, and D^m the dipolar interaction at full alignment, $D^m = -(\mu_0\hbar\gamma_H\gamma_N/8\pi^2)(r_{HN})^{-3}$. γ_H and γ_N are the gyromagnetic ratios of ^{1}H and ^{15}N, μ_0 is the permeability of free space, $\hbar$ is Planck's constant, and r_{HN} is the average internuclear distance. For $^1D_{HN}$ couplings, $D^m \sim 21.7$ kHz. [c] Euler angles (α, β, γ) describing the orientation of the unique alignment axis A_{zz} in the inertial frame of IFNAR2-EC. Because of the 2-fold-degeneracy of the alignment tensor, the effective angle between unique axes of the inertia and alignment tensors is ∼8°. [d] Errors were estimated using Monte Carlo simulations.

by low order parameters ($S^2 \sim 0.6$). In the interdomain helix (residues W100−D104), residues W100−L101 are located in the hydrophobic core of the N-domain and are rigid, while residues A102−I103 are more exposed. Overall, the microdynamic parameters are consistent with secondary structure elements of the previously determined structure.

Residual Dipolar Coupling Analysis. RDCs for backbone ^{1}H-^{15}N moieties were measured using an ^{15}N-labeled IFNAR2-EC sample in compressed polyacrylamide gel. Because of spectral overlap only 125 such couplings could be determined unambiguously. Couplings were weighted by a factor of 1/*S*, with *S* representing the estimated order parameter at 800 MHz. After exclusion of 12 couplings from unstructured regions of IFNAR2-EC and three outliers, 110 couplings entered the final analysis (Figure 5, top). The best-fitting alignment tensor for these couplings has a magnitude of $D = 6.3 \pm 0.4$ Hz and a rhombicity of $R = 0.56 \pm 0.08$, and its long axis forms an angle of 8° with the principal inertia axis of IFNAR2-EC.

The angular dependence of RDCs can be used to establish relative domain orientations in multidomain proteins. The RDC data was split into N-domain (residues 1−106, 52 couplings) and C-domain (residues 107−212, 58 couplings) sets, each of which were independently fitted to an optimal alignment tensor. As shown in Table 4, these alignment tensors describing subsets of the original data show only small variations when compared to the overall alignment tensor. Error analysis indicates that the introduction of two new parameters (magnitude and rhombicity of the second tensor) is not statistically justified. The collinearity of the alignment frames for both domains is further demonstrated in Figure 5, as back-calculated values using the single-domain and overall alignment tensors could not be distinguished. Moreover, the root-mean-square deviation (rmsd) between back-calculated values from the single-domain alignment tensors is under 1 Hz. Overall, RDC data confirm the relative perpendicular orientation observed between the two domains of IFNAR2-EC, and indicate that they tumble in solution as a rigid body with no flexibility at the interdomain hinge.

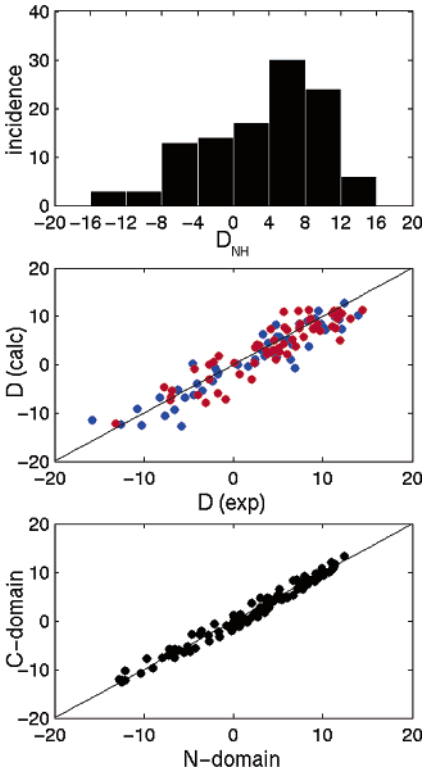

FIGURE 5: RDCs in IFNAR2-EC support hinge rigidity. Top, histogram showing the characteristic distribution of RDCs. Middle, correlation between measured (D_{exp}) and calculated (D_{calc}) RDCs of IFNAR2-EC based upon the alignment tensor of the entire molecule. RDCs of the N- and C-domains are shown as blue and red markers, respectively. The rmsd value is 2.6 Hz. Bottom, RDC values back-calculated from the N-domain tensor are plotted against those back-calculated from the C-domain tensor. The rmsd between the two back-calculated sets is under 1 Hz. Collinearity of the two single-domain tensors strongly suggests that the two domains tumble as a single body, and are rigidly linked at the interdomain hinge.

DISCUSSION

It is commonly accepted that only a combination of structural and dynamic factors can comprehensively account for protein function. One of the great advantages of NMR-based structural study of proteins is the ability to examine them in their native environment and follow dynamic processes, rather than describe a snapshot selected from a variety of possible conformations. IFNAR2-EC presented a challenging system for ^{15}N relaxation measurements, due to limited sample concentrations and basic pH measurement conditions. Here we use the model-free approach to analyze ^{15}N spin relaxation measurements and describe the backbone dynamics of IFNAR2-EC, a first study of its kind for a cytokine receptor. Model-free analysis is also a prerequisite for accurate interpretation of RDC measurements. Since picosecond to nanosecond motions in the protein backbone affect its average orientation, the observed residual couplings are modulated by backbone order parameters. Moreover, RDC-based refinement of interdomain orientations requires corroborative evidence excluding mobility at the interface between domains. It is therefore the combination of ^{15}N spin

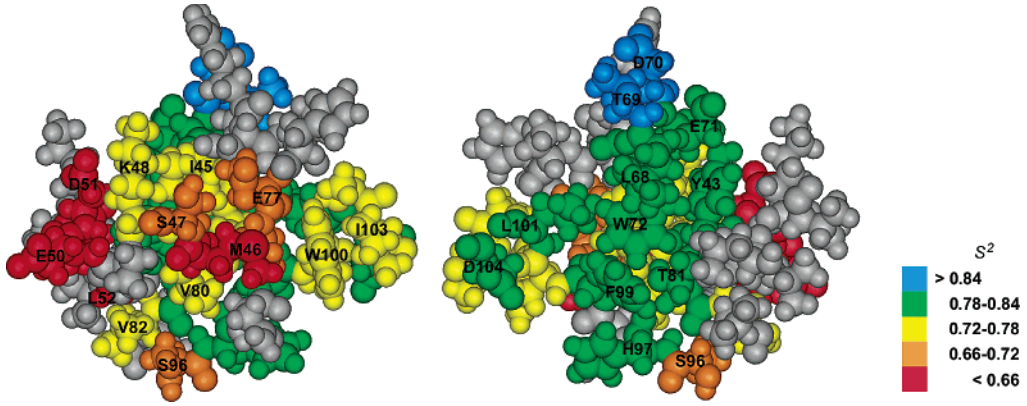

FIGURE 6: Dynamics of the ligand binding site upon IFNAR2-EC. Backbone order parameters (S^2) are plotted in color-code upon the ligand binding site of IFNAR2-EC, revealing two distinct surfaces. Left (front view), the surface of the CC′FG$_N$ β-sheet directly interacts with the IFN ligand and exhibits some mobility, with an average value of $S^2 = 0.72$. Right (reverse view), the opposite surface of the CC′FG$_N$ β-sheet stabilizes the binding site conformation and is more rigid, averaging $S^2 = 0.82$. IFNAR2-EC residues on both surfaces are labeled. S^2 values represent an average between calculated order parameters at both fields. Each color step spans two standard deviations in the value of S^2.

relaxation and RDC measurements that validates our conclusions regarding IFNAR2-EC.

Model-Free Analysis of IFNAR2-EC. Model-free analysis describes molecular motions on the picosecond to nanosecond time scale. Longer microsecond to millisecond scale motions are identified through the conformational exchange contribution, R_{ex}, to R_2. At pH 8.0, this phenomenological parameter absorbs the effects of solvent exchange broadening, as well as various errors accumulated throughout the calculation. Since at pH 8.0 solvent exchange rates for proteins with well-defined secondary structure are typically $10^{-4}-10^{-1}$ min^{-1} (*63*), amide protons of IFNAR2-EC are at the slow-exchange limit. Nevertheless, R_{ex} must be considered less reliable than S^2 and τ_i, as has been suggested previously (*64*). Model-free analysis of IFNAR2-EC was conducted following commonly accepted model selection protocols for data acquired at 500 and 800 MHz. The values of S^2 are typically higher at 800 MHz, differing from those at 500 MHz by 1−2 standard deviations. This phenomenon has been previously observed (*54*), and may originate from the manner in which the model-free approach addresses local dynamics, particularly at higher fields (*65*). Generally, the fitting is more discriminating at 500 MHz than at 800 MHz. However, the profile of order parameters and model selection, as well as the qualitative description of IFNAR2-EC mobility emerging from both datasets, are very similar in both datasets.

Dynamics of the IFNAR2-EC Binding Site. The type I IFN binding site is formed by three segments of IFNAR2-EC, the CC′$_N$ (residues 45−52) and EF$_N$ (residues 74−82) loops and the interdomain helix (residues 100−104). Model-free analysis for these segments underlines their relative mobility. In the CC′$_N$ loop residues 50−52 are fitted to model 5 with S^2 values in the 0.5−0.6 range. In the EF$_N$ loop residues E77 and A78 are assigned to model 5, and the mobility of residues T75 and H76 is evidenced by their absence from the ^{1}H-^{15}N HSQC spectrum of IFNAR2-EC. These two loops form an alternating charge motif shown to interact with a congruent pattern upon IFNα2 (*22*). Mobility of this region allows the receptor binding site to adopt an optimal conformation for binding its ligands.

We have previously suggested the IFNAR2-EC binding site to comprise of two hydrophobic surfaces, the anterior face which interacts with the incoming ligand, and the posterior face which maintains the integrity of the binding site (*22*). Backbone dynamics provide a first quantitative distinction between these two surfaces, as demonstrated strikingly in Figure 6. Average S^2 values for residues in the anterior face (including residues M46, L52, A78, V80, W100, and I103) are 0.70 ± 0.03 (0.74 ± 0.03), and for residue of the posterior face (including Y43, I45, L68, W72, Y79, F99, and L101) 0.79 ± 0.03 (0.86 ± 0.03) for the 11.74 (18.79) T data. This description of an "adaptable" binding site buttressed by a rigid support is consistent with several previous observations. The extensive hydrophobic patch in the IFNAR2-EC binding site and its aliphatic character hint to an ability to accommodate various ligands (*22*). Amide proton temperature coefficient measurements (data not shown) and previous solvent exchange experiments suggest that ligand binding is accompanied by a rigidification which is propogated by the FNIII domain to residues outside the binding site (*26*). Moreover, a malleable binding site would account for our previous observation that inter-β-strand NOE interactions were generally weaker than typical distances in secondary structure elements would predict (Chill and Anglister, unpublished results). It is important to note that while our study focuses upon backbone dynamics, several of the receptor−ligand interactions involve side-chain groups. However, the qualitative description presented here remains valid, since backbone dynamics of the IFNAR2-EC binding site reflect the roles played by the various residues that contribute to its structure and function.

The Interdomain Hinge Is Rigid. In IFNAR2-EC the hinge region is formed by the AB$_N$ β-hairpin (residues 16−22), and the F$_C$ β-strand and FG$_C$ loop (residues 183−185, 194−196) packing against the hinge segment itself (residues 104−111). This region forms direct contacts with the structural cores of the two FNIII domains, together forming a hydrophobic domain which spans the entire receptor (*22*). Model-free analysis of IFNAR2-EC is the first to provide quantitative experimental evidence that the hinge region is rigid, as the vast majority of its residues were associated with rigid models in the analysis, and none were associated with significant internal motion or the Clore extended model. Structural similarities of cytokine receptor hinge regions, which are typically an extensive hydrophobic interface with

a total buried area of 1000−1100 Å^2, strongly indicate that interdomain rigidity is common to this receptor superfamily. Indeed, temperature factors for the hinge region of human tissue factor were consistent with a rigid structure (*66*). Obtained for a soluble protein, this conclusion carries special significance, since structures determined by crystallography, particularly those of multidomain proteins, may suffer from crystal packing effects. Notable in this respect is the finding of different interdomain angles for two molecules of the asymmetric unit (*18*, *67*).

Further evidence for the rigidity of the hinge region and perpendicular interdomain angle in IFNAR2-EC is offered by its diffusional anisotropy and RDC measurements. Independent fitting of RDC data from each FNIII domain resulted in approximately collinear alignment tensors with highly similar magnitudes, whereas a flexible hinge region would dictate an averaging of RDCs and poorly correlated tensors. Analysis of R_2/R_1 ratios and their interpretation in terms of IFNAR2-EC rotational diffusion further substantiate the rigidity of the hinge region. Statistically insignificant differences in τ_C and $D_\parallel/D_\perp$ were observed for the two tensors independently fitted to N- and C-domain R_2/R_1 ratios. Moreover, these tensors were mutually collinear, and their unique axes formed an angle of ∼15° with the unique inertia axis of IFNAR2-EC, whereas a rotation of 45−50° was necessary to co-align them with the unique inertia axes of the single FNIII domains. As diffusion is closely related to molecular shape, this result strongly supports the hypothesis of rigidly linked, rather than independently tumbling, perpendicular FNIII domains. Overall, ^{15}N spin relaxation and RDC measurements of IFNAR2-EC provide conclusive evidence for a rigidly held two-domain structure for IFNAR2-EC.

Implications for Cytokine Signaling. Signaling throughout the cytokine superfamily is contingent upon formation of a productive ternary complex between the extracellular domains of the two receptor subunits and the ligand. This study offers the first opportunity to study a member of this receptor family in solution and unliganded form, illuminating the dynamic factors that underlie the initiation of the signaling cascade. First, our results reveal a ligand binding site comprised of alternating charged residues mounted upon mobile loops and an extensive malleable hydrophobic binding surface. The aliphatic character of the IFNAR2-EC surface interacting with the ligand further contributes to the versatility of the receptor. In the case of IFNAR2 this adaptability may explain the observed cross-reactivity with multiple ligands. Second, we have established that the interdomain hinge is rigid. In light of these results, and in conjunction with the lack of ligand-induced chemical shifts in the hinge region (*26*), it seems highly unlikely that IFN signaling involves any change in interdomain orientation, contrary to previous claims (*67*).

In the context of the ternary signaling complex, hinge rigidity ensures the correct orientation of the initially formed IFNAR2/IFN complex relative to the incoming IFNAR1. A contact surface between C-domains of the receptor subunits has been established for the class I receptors GHR, EPOR, and PRLR, and has not been excluded for IFNAR. More importantly, due to the rigid hinge, variations in the orientation of receptor extracellular domains modulate the relative positioning of kinases in the cytoplasm, thereby controlling the rate and efficiency of phosphorylation. Studies of various EPOR complexes have provided compelling evidence that optimal receptor orientation in the ternary signaling complex is essential for signal transduction (*68*, *69*). This mechanism may also contribute to ligand-specific signaling pathways. Subtle variations in the signaling complexes formed with IFNα and IFNβ may be transformed by the rigidly held C-domain into different relative orientations of the cellular participants of the signaling cascade. This could explain the ligand-specific cellular responses to IFN binding.

ACKNOWLEDGMENT

We are indebted to Mrs. Rina Levy for expression and purification of ^{15}N-IFNAR2-EC and U-IFNα2. We are thankful to Prof. D. Fushman (University of Maryland, College Park) for his valuable comments, as well as making software programs ROTDIFF and DYNAMICS available to us. We are grateful to Prof. E. Meirovitch (Bar-Ilan University) for several helpful discussions and critical reading of the manuscript, and acknowledge Dr. Y. Shapiro (Bar-Ilan University), Prof. Gideon Schreiber (Weizmann Institute of Science), and Dr. Vitali Tugarinov (U. Toronto) for useful remarks. S.Q. is the recipient of a Ph.D. Minerva Fellowship.

SUPPORTING INFORMATION AVAILABLE

R_1, R_2, and ^{15}N-{^{1}H} NOE data measured at 11.74 T (Supplement 1) and 18.79 T (Supplement 2), and model-free analysis of relaxation data at 11.74 T (Supplement 3) and 18.79 T (Supplement 4), including a comparison to backbone rmsd values. This material is available free of charge via the Internet at http://pubs.acs.org.

REFERENCES

1. Stark, G. R., Kerr, I. M., Williams, B. R., Silverman, R. H., and Schreiber, R. D. (1998) How cells respond to interferons, *Annu. Rev. Biochem. 67*, 227−264.
2. Tossing, G. (2001) New developments in interferon therapy, *Eur. J. Med. Res. 6*, 47−65.
3. Luxon, B. A., Grace, M., Brassard, D., and Borden, R. (2002) Pegylated interferons for the treatment of chronic hepatitis C infection, *Clin. Ther. 24*, 1363−1383.
4. Bukowski, R., Tendler, C., Cutler, D., Rose, E., Laughlin, M., and Statkevich, P. (2002) Treating cancer with PEG intron: pharmakinetic profile and dosing guidelines for an improved interferon-α2b formulation, *Cancer 95*, 389−396.
5. Kirkwood, J. (2002) Cancer immunotherapy: the interferon-α experience, *Semin. Oncol. 29*, 18−26.
6. Deonarain, R. D., Chan, D. C. M., Platanias, L. C., and Fish, E. N. (2002) Interferon α/β receptor interactions: a complex story unfolding, *Curr. Pharm. Des. 8*, 99−110.
7. Wong, T., Majchrzak, B., Bogoch, E., Keystone, E. C., and Fish, E. N. (2003) Therapeutic implications for interferon-α in arthritis: a pilot study, *J. Rheumatol. 30*, 934−940.
8. Uze, G., Lutfalla, G., and Gresser, I. (1990) Genetic transfer of a functional human interferon a receptor into mouse cells: cloning and expression of its cDNA, *Cell 60*, 225−234.
9. Novick, D., Cohen, B., and Rubinstein, M. (1994) The human interferon α/β receptor: characterization and molecular cloning, *Cell 77*, 391−400.
10. Bazan, J. F. (1990) Structural design and molecular evolution of a cytokine receptor superfamily, *Proc. Natl. Acad. Sci. U.S.A. 87*, 6934−6938.
11. Cohen, B., Novick, D., Barak, S., and Rubinstein, M. (1995) Ligand-induced association of the type I interferon receptor components, *Mol. Cell. Biol. 15*, 4208−4214.
12. Uze, G., Lutfalla, G., and Mogensen, K. E. (1995) α- and β-interferons and their receptor and their friends and relations, *J. Interferon Cytokine Res. 15*, 3−26.

13. de Vos, A. M., Ultsch, M., and Kossiakoff, A. A. (1992) Human growth hormone and extracellular domain of its receptor: crystal structure of the complex, *Science 255*, 306−312.
14. Somers, W., Ultsch, M. H., de Vos, A. M., and Kossiakoff, A. A. (1994) The X-ray structure of a growth hormone-prolactin receptor complex, *Nature 372*, 478−481.
15. Livnah, O., Stura, E. A., Johnson, D. L., Middleton, S. A., Mulcahy, L. S., Wrighton, N. C., Dower, W. J., Jolliffe, L. K., and Wilson, I. A. (1996) Functional mimicry of a protein hormone by a peptide agonist: the EPO receptor complex at 2.8 Å, *Science 273*, 464−471.
16. Josephson, K., Logsdon, N. J., and Walter, M. R. (2001) Crystal structure of the IL-10/IL-10R1 complex reveals a shared receptor binding site, *Immunity 15*, 35−46.
17. Walter, M. R., Windsor, W. T., Nagabhushan, T. L., Lundell, D. J., Lunn, C. A., Zauodny, P. J., and Narula, S. K. (1995) Crystal structure of a complex between interferon-γ and its soluble high-affinity receptor, *Nature 376*, 230−235.
18. Elkins, P. A., Christinger, H. W., Sandowski, Y., Sakal, E., Gertler, A., de Vos, A. M., and Kossiakoff, A. A. (2000) Ternary complex between placental lactogena and the extracellular domain of the prolactin receptor, *Nat. Struct. Biol. 7*, 808−815.
19. Randall, M., and Kossiakoff, A. A. (2001) The structure and activity of a monomeric interferon-γ:α-chain receptor signaling complex, *Structure 9*, 155−163.
20. Feher, V. A., and Cavanagh, J. (1999) Millisecond-time scale motions contribute to the function of the bacterial response regulator protein Spo0F, *Nature 400*, 289−293.
21. Piehler, J., and Schreiber, G. (1999). Biophysical analysis of the interaction of human ifnar2 expressed in E. coli with IFNα2, *J. Mol. Biol. 289*, 57−67.
22. Chill, J. H., Quadt, S. R., Levy, R., Schreiber, G. E., and Anglister, J. (2003) NMR structure of the human type I interferon receptor reveals the molecular basis for ligand binding, *Structure (Camb.) 11*, 791−802.
23. Piehler, J., and Schreiber, G. (1999) Mutational and structural analysis of the binding interface between type I interferons and their receptor Ifnar2, *J. Mol. Biol. 294*, 223−37.
24. Lewerenz, M., Mogensen, K. E., and Uze, G. (1998) Shared receptor components but distinct complexes for α and β interferons, *J. Mol. Biol. 282*, 585−599.
25. Chuntharapai, A., Gibbs, V., Lu, J., Ow, A., Marsters, S., Ashkenazi, A., De Vos, A., and Jin Kim, K. (1999) Determination of residues involved in ligand binding and signal transmission in the human IFN-α receptor 2, *J. Immunol. 163*, 766−773.
26. Chill, J. H., Nivasch, R., Levy, R., Albeck, S., Schreiber, G. E., and Anglister, J. (2002). The human interferon receptor: NMR-based modeling of the IFN-α2 binding site, and observed ligand-induced tightening, *Biochemistry 41*, 3575−3585.
27. Runkel, L., Pfeffer, L., Lewerenz, M., Monneron, D., Yang, C. H., Murti, A., Pellegrini, S., Goelz, S., Uze, G., and Mogensen, K. (1998) Differences in activity between alpha and beta type I interferons explored by mutational analysis, *J. Biol. Chem. 273*, 8003−8.
28. Mogensen, K. E., Lewerenz, M., Reboul, J., Lutfalla, G., and Uze, G. (1999) The type I interferon receptor: structure, function, and evolution of a family business, *J. Interferon Cytokine Res. 19*, 1069−1098.
29. Abramovich, C., Shulman, L. M., Ratovitski, E., Harroch, S., Tovey, M., Eid, P., and Revel, M. (1994) Differential tyrosine phosphorylation of the IFNAR chain of the type I interferon receptor and of an associated surface protein in response to IFN-α and IFN-β, *EMBO J. 13*, 5871−5877.
30. Russell-Harde, D., Wagner, T. C., Perez, H. D., and Croze, E. (1999) Formation of a uniquely stable type I interferon receptor complex by interferon-β is dependent upon particular interactions between interferon-β and its receptor and independent of tyrosine phosphorylation, *Biochem. Biophys. Res. Commun. 255*, 539−544.
31. Kay, L. E. (1998) Protein dynamics from NMR, *Biochem. Cell Biol. 76*, 145−152.
32. Palmer, A. G. I. (2001) NMR probes of molecular dynamics: overview and comparison with other techniques, *Annu. Rev. Biophys. Biomol. Struct. 30*, 129−155.
33. Bruschweiler, R. (2003) New approaches for the dynamic interpretation and prediction of NMR relaxation data from proteins, *Curr. Opin. Struct. Biol. 13*, 175−183.
34. Lipari, G., and Szabo, A. (1982) Model free approach to the interpretation of nuclear magnetic resonance relaxation in macromolecules. 1. Theory and range of validity. 2. Analysis of experimental results, *J. Am. Chem. Soc. 104*, 4546−4570.
35. Clore, G. M., Driscoll, P. C., Wingfield, P. T., and Gronenborn, A. M. (1990) Analysis of the backbone dynamics of interleukin-1 β using two-dimensional inverse detected heteronuclear ^{15}N-^{1}H NMR spectroscopy *Biochemistry 29*, 7387−7401.
36. Sass, H.-J., Musco, G., Stahl, S., Wingfield, P. T., and Grzesiek, S. (2000) Solution NMR of proteins within polyacrylamide gels: diffusional properties and residual alignment by mechanical stress or embedding of oriented purple membranes, *J. Biomol. NMR 18*, 303−309.
37. Tycko, R., Blanco, F. J., and Ishii, Y. (2000) Alignment of biopolymers in strained gels: a new way to create detectable dipole-dipole couplings in high-resolution biomolecular NMR, *J. Am. Chem. Soc. 122*, 9340−9341.
38. Marion, D., and Wuthrich, K. (1983) Application of phase-sensitive two-dimensional correlated spectroscopy (COSY) for the measurement of ^{1}H-^{1}H spin−spin coupling constants, *Biochem. Biophys. Res. Commun. 113*, 967−974.
39. Sklenar, V., Piotto, M., Leppik, R., and Saudek, V. (1993) Gradient-tailored water suppression for ^{1}H-^{15}N HSQC experiments optimized to retain full sensitivity, *J. Magn. Reson. Ser. A 102*, 241−245.
40. Bax, A., and Subramanian, J. (1986) Sensitivity-enhanced two-dimensional shift correlation NMR spectroscopy, *J. Magn. Reson. 67*, 565−570.
41. Delaglio, F., Grzesiek, S., Vuister, G. W., Zhu, G., Pfeifer, J., and Bax, A. (1995) NMRPipe: a multidimensional spectral processing system based on UNIX pipes, *J. Biomol. NMR. 6*, 277−293.
42. Kay, L. E., Nicholson, L. K., Delaglio, F., Bax, A., and Torchia, D. A. (1992)Pulse sequences for removal of the effects of cross-correlation between dipolar and chemical-shift anisotropy relaxation mechanism on the measurement of heteronuclear T1 and T2 values in proteins, *J. Magn. Res. 97*, 359−375.
43. Palmer, A. G., Rance, M., and Wright, P. E. (1992) Suppression of the effects of cross-correlation between dipolar and anisotropic chemical shift relaxation mechanisms in the measurement of spin−spin relaxation rates, *Mol. Phys. 75*, 699−711.
44. Grzesiek, S., and Bax, A. (1993) The importance of not saturating H_2O in protein NMR − application to sensitivity enhancement and NOE measurements, *J. Am. Chem. Soc. 115*, 12593−12594.
45. Grzesiek, S., Bax, A., Hu, J. S., Kaufman, J., Palmer, I., Stahl, S. J., Tjandra, N., and Wingfield, P. T. (1997) Refined solution structure and backbone dynamics of HIV-1 Nef, *Protein Sci. 6*, 1248−1263.
46. Garcia de la Torre, J., Huertas, M. L., and Carrasco, N. (2000) HYDRONMR: Prediction of NMR relaxation of globular proteins from atomic-level structures and hydrodynamic calculations, *J. Magn. Res. 147*, 138−146.
47. Franks, F. (1988) *Characterization of Proteins*, pp 70−71, Humana Press, Clifton, NJ.
48. Kay, L. E., Torchia, D. A., and Bax, A. (1989) Backbone dynamics of proteins as studied by 15N inverse detected heteronuclear NMR spectroscopy: application to staphylococcal nuclease, *Biochemistry 28*, 8972−9.
49. Lee, L. K., Rance, M., Chazin, W. J., and Palmer, A. G. (1997) Rotational diffusion anisotropy of proteins from simultaneous analysis of ^{15}N and ^{13}Cα nuclear spin relaxation, *J. Biomol. NMR 9*, 287−298.
50. Tjandra, N., Feller, S. E., Pastor, R. W., and Bax, A. (1995) Rotational diffusion anisotropy of human ubiquitin from ^{15}N NMR relaxation, *J. Am. Chem. Soc. 117*, 12562−12566.
51. Fushman, D., Xu, R., and Cowburn, D. (1999) Direct determination of changes of interdomain orientation on ligation: use of the orientational dependence of ^{15}N NMR relaxation in Abl SH(32), *Biochemistry 38*, 10225−10230.
52. Dosset, P., Hus, J. C., Blackledge, M., and Marion, D. (2000) Efficient analysis of macromolecular rotational diffusion from heteronuclear relaxation data, *J. Biomol. NMR 16*, 23−28.
53. Abragam, A. (1961) *Principles of Nuclear Magnetism*, Clarendon Press, Oxford.
54. Vugmeyster, L., Trott, O., McKnight, C. J., Raleigh, D. P., and Palmer, A. G. (2002) Temperature-dependent dynamics of the villin headpiece subdomain, an unusually small thermostable protein, *J. Mol. Biol. 320*, 841−854.

55. Fushman, D., Cahill, S., and Cowburn, D. (1997) The main chain dynamics of the dynamin Plecksrin Homology (PH) domain in solution: analysis of ^{15}N-relaxation with monomer−dimer equilibration, *J. Mol. Biol. 266*(1), 273−294.
56. Hall, J. B., and Fushman, D. (2003) Characterization of the overall and local dynamics of a protein with intermediate rotational anisotropy: differentiating between conformational exchange and anisotropic diffusion in the B3 domain of protein G, *J. Biomol. NMR 24*.
57. Mandel, A. M., Akke, M., and Palmer, A. G. (1995) Backbone dynamics of *Escherichia coli* ribonuclease HI: correlations with structure and function in an active enzyme, *J. Mol. Biol. 246*, 144−63.
58. Cordier, F., Dingley, A. J., and Grzesiek, S. (1999) A doublet-separated sensitivity-enhanced HSQC for the determination of scalar and dipolar one-bond J-couplings, *J. Biomol. NMR 13*, 175−180.
59. Johnson, B. A., and Blevins, R. A. (1994) NMRView − a computer program for analysis and visualization of NMR data, *J. Biomol. NMR 4*, 603−614.
60. Dosset, P., Hus, J. C., Marion, D., and Blackledge, M. (2001) A novel interactive tool for rigid-body modeling of multi-domain macromolecules using residual dipolar couplings, *J. Biomol. NMR 20*, 223−231.
61. Copie, V., Tomita, Y., Akiyama, S. K., Aota, S., Yamada, K. M., Venable, R. M., Pastor, R. W., Krueger, S., and Torchia, D. A. (1998) Solution structure and dynamics of liked cell attachment modules of mouse fibronectin containing the RGD and synergy regions: comparison with the human fibronectin crystal structure, *J. Mol. Biol. 277*, 663−682.
62. Bernado, P., Garcia de la Torre, J., and Pons, M. (2002) Interpretation of ^{15}N NMR relaxation data of globular proteins using hydrodynamic calculations with HYDRONMR, *J. Biomol. NMR 23*, 139−150.
63. Bai, Y., Englander, J. J., Mayne, L., Milne, J. S., and Englander, S. W. (1995) Thermodynamic parameters from hydrogen exchange measurements, *Methods Enzymol. 259*, 344−356.
64. McCallum, S. A., Hitchens, T. K., Torborg, C., and Rule, G. S. (2000) Ligand-induced changes in the structure and dynamics of a human class μ-glutathione S-transferase, *Biochemistry 39*, 7343−7356.
65. Tugarinov, V., Liang, Z., Shapiro, Y. E., Freed, J. H., and Meirovitch, E. (2001) A structural mode-coupling approach to ^{15}N NMR relaxation in proteins, *J. Am. Chem. Soc. 123*, 3055−3063.
66. Muller, Y. A., Ultsch, M. H., and de Vos, A. M. (1996) The crystal structure of the extracellular domain of human tissue factor refined to 1.7 Å resolution, *J. Mol. Biol. 256*, 144−159.
67. Muller, Y. A., Kelley, R. F., and de Vos, A. M. (1998) Hinge bending within the cytokine receptor superfamily revealed by the 2.4 Å crystal structure of the extracellular domain of rabbit tissue factor, *Protein Sci. 7*, 1106−1115.
68. Syed, R. S., Reid, S. W., Li, C., Cheetham, J. C., Aoki, K. H., Liu, B., Zhan, H., Osslund, T. D., Chirino, A. J., Zhang, J., Finer-Moore, J., Elliott, S., Sitney, K., Katz, B. A., Matthews, D. J., Wendoloski, J. J., Egrie, J., and Stroud, R. M. (1998) Efficiency of signaling through cytokine receptors depends critically on receptor orientation, *Nature 395*, 511−516.
69. Constantinescu, S. N., Huang, L. J., Nam, H., and Lodish, H. F. (2001) The erythropoietin receptor cytosolic juxtamembrane domain contains an essential, precisely oriented, hydrophobic motif, *Mol. Cell, 7*, 377−385.

BI049606G